RESEARCH ARTICLE SUMMARY

PLANETARY SCIENCE

Surface compositions across Pluto and Charon

W. M. Grundy,* R. P. Binzel, B. J. Buratti, J. C. Cook, D. P. Cruikshank, C. M. Dalle Ore, A. M. Earle, K. Ennico, C. J. A. Howett, A. W. Lunsford, C. B. Olkin, A. H. Parker, S. Philippe, S. Protopapa, E. Quirico, D. C. Reuter, B. Schmitt, K. N. Singer, A. J. Verbiscer, R. A. Beyer, M. W. Buie, A. F. Cheng, D. E. Jennings, I. R. Linscott, J. Wm. Parker, P. M. Schenk, J. R. Spencer, J. A. Stansberry, S. A. Stern, H. B. Throop, C. C. C. Tsang, H. A. Weaver, G. E. Weigle II, L. A. Young, and the New Horizons Science Team

INTRODUCTION: The Kuiper Belt hosts a swarm of distant, icy objects ranging in size from small, primordial planetesimals to much larger, highly evolved objects, representing a whole new class of previously unexplored cryogenic worlds. Pluto, the largest among them, along with its system of five satellites, has been revealed by NASA's New Horizons spacecraft flight through the system in July 2015, nearly a decade after its launch.

RATIONALE: Landforms expressed on the surface of a world are the product of the available materials and of the action of the suite of processes that are enabled by the local physical and chemical conditions. They provide observable clues about what processes have been at work over the course of time, the understanding of which is a prerequisite to reconstructing the world's history. Materials known to exist at Pluto's surface from ground-based spectroscopic observations include highly volatile cryogenic ices of N_2 and CO, along with somewhat less volatile CH_4 ice, as well as H_2O and C_2H_6 ices and more complex tholins that are inert at Pluto surface temperatures. Ices of H_2O and NH_3 are inert components known to exist on Pluto's large satellite Charon. New Horizons' Ralph instrument was designed to map colors and compositions in the Pluto system. It consists of a charge-coupled device camera with four color filters spanning wavelengths from 400 to 970 nm plus a near-infrared imaging spectrometer covering wavelengths from 1.25 to 2.5 μm, where the various cryogenic ices are distinguishable via their characteristic vibrational absorption features.

RESULTS: New Horizons made its closest approach to the system on 14 July 2015. Observations of Pluto and Charon obtained that day reveal regionally diverse colors and compositions. On Pluto, the color images show nonvolatile tholins coating an ancient, heavily cratered equatorial belt. A smooth, thousand-kilometer plain must be able to refresh its surface rapidly enough to erase all impact craters. Infrared observations of this region show volatile ices including N_2 and CO. H_2O ice is not detected there, but it does appear in neighboring regions. CH_4 ice appears on crater rims and mountain ridges at low latitudes and is abundant at Pluto's high northern latitudes. Pluto's regional albedo contrasts are among the most extreme for solar system objects. Pluto's large moon Charon offers its own surprises. Its H_2O ice–rich surface is unlike other outer solar system icy satellites in exhibiting distinctly reddish tholin coloration around its northern pole as well as a few highly localized patches rich in NH_3 ice.

ON OUR WEB SITE

Read the full article at http://dx.doi.org/10.1126/science.aad9189

CONCLUSION: Pluto exhibits evidence for a variety of processes that act to modify its surface over time scales ranging from seasonal to geological. Much of this activity is enabled by the existence of volatile ices such as N_2 and CO that are easily mobilized even at the extremely low temperatures prevalent on Pluto's surface, around 40 K. These ices sublimate and condense on seasonal time scales and flow glacially. As they move about Pluto's surface environment, they interact with materials such as H_2O ice that are sufficiently rigid to support rugged topography. Although Pluto's durable H_2O ice is probably not active on its own, it appears to be sculpted in a variety of ways through the action of volatile ices of N_2 and CO. CH_4 ice plays a distinct role of its own, enabled by its intermediate volatility. CH_4 ice condenses at high altitudes and on the winter hemisphere, contributing to the construction of some of Pluto's more unusual and distinctive landforms. The latitudinal distribution of Charon's polar reddening suggests a thermally controlled production process, and the existence of highly localized patches rich in NH_3 ice on its surface implies relatively recent emplacement. ■

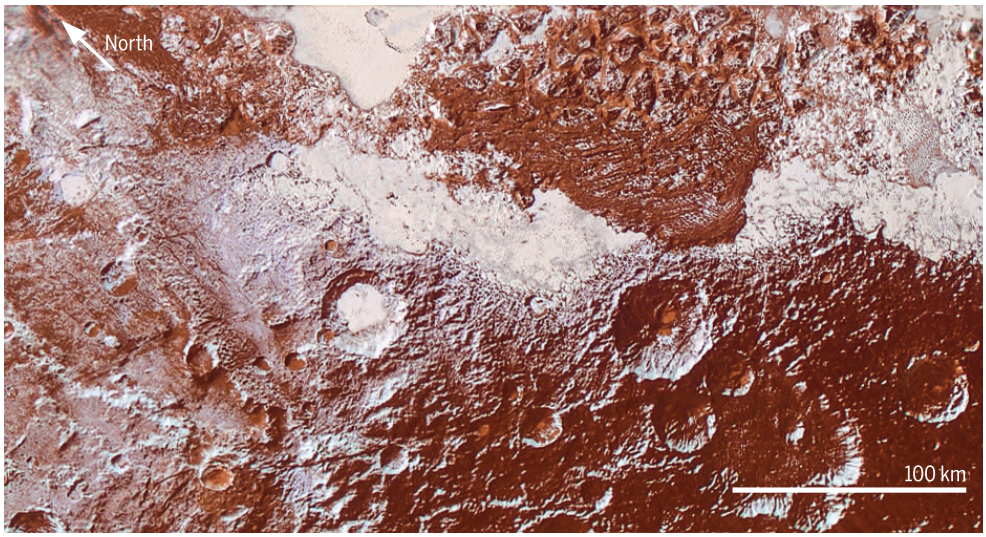

Enhanced color view of Pluto's surface diversity. This mosaic was created by merging Multispectral Visible Imaging Camera color imagery (650 m per pixel) with Long Range Reconnaissance Imager panchromatic imagery (230 m per pixel). At lower right, ancient, heavily cratered terrain is coated with dark, reddish tholins. At upper right, volatile ices filling the informally named Sputnik Planum have modified the surface, creating a chaos-like array of blocky mountains. Volatile ice occupies a few nearby deep craters, and in some areas the volatile ice is pocked with arrays of small sublimation pits. At left, and across the bottom of the scene, gray-white CH_4 ice deposits modify tectonic ridges, the rims of craters, and north-facing slopes.

The list of author affiliations is available in the full article online.
*Corresponding author. E-mail: w.grundy@lowell.edu
Cite this article as W. M. Grundy *et al.*, Science 351, aad9189 (2016). DOI: 10.1126/science.aad9189

RESEARCH ARTICLE

PLANETARY SCIENCE

Surface compositions across Pluto and Charon

W. M. Grundy,[1]* R. P. Binzel,[2] B. J. Buratti,[3] J. C. Cook,[4] D. P. Cruikshank,[5] C. M. Dalle Ore,[5,6] A. M. Earle,[2] K. Ennico,[5] C. J. A. Howett,[4] A. W. Lunsford,[7] C. B. Olkin,[4] A. H. Parker,[4] S. Philippe,[8] S. Protopapa,[9] E. Quirico,[8] D. C. Reuter,[7] B. Schmitt,[8] K. N. Singer,[4] A. J. Verbiscer,[10] R. A. Beyer,[5,6] M. W. Buie,[4] A. F. Cheng,[11] D. E. Jennings,[7] I. R. Linscott,[12] J. Wm. Parker,[4] P. M. Schenk,[13] J. R. Spencer,[4] J. A. Stansberry,[14] S. A. Stern,[4] H. B. Throop,[15] C. C. C. Tsang,[4] H. A. Weaver,[11] G. E. Weigle II,[16] L. A. Young,[4] and the New Horizons Science Team

The New Horizons spacecraft mapped colors and infrared spectra across the encounter hemispheres of Pluto and Charon. The volatile methane, carbon monoxide, and nitrogen ices that dominate Pluto's surface have complicated spatial distributions resulting from sublimation, condensation, and glacial flow acting over seasonal and geological time scales. Pluto's water ice "bedrock" was also mapped, with isolated outcrops occurring in a variety of settings. Pluto's surface exhibits complex regional color diversity associated with its distinct provinces. Charon's color pattern is simpler, dominated by neutral low latitudes and a reddish northern polar region. Charon's near-infrared spectra reveal highly localized areas with strong ammonia absorption tied to small craters with relatively fresh-appearing impact ejecta.

NASA's New Horizons probe explored the Pluto system in July 2015, returning data from instruments sensitive to electromagnetic radiation from ultraviolet through radio wavelengths, as well as to charged particles and dust (*1*, *2*). Since the publication of initial results (*3*), more data have been transmitted to Earth. This paper focuses on the spectral and spatial dependence of sunlight reflected from Pluto and Charon in the wavelength range 400 to 2500 nm. These wavelengths are useful for investigating the cryogenic ices prevalent on their surfaces. We restrict our attention to the encounter hemispheres of both bodies because data for the non-encounter hemispheres are as yet incomplete and have lower spatial resolution. Accompanying papers in this issue present results on geology (*4*), atmospheres (*5*), the particle environment (*6*), and small satellites (*7*).

Instrument overview

Data in this paper were chiefly obtained with New Horizons' Ralph instrument (*8*). Ralph consists of a single *f*/8.7 telescope with a 658-mm effective focal length that feeds light to two focal planes: (i) the Multispectral Visible Imaging Camera (MVIC), a visible/near-infrared (NIR) panchromatic and color imager, and (ii) the Linear Etalon Imaging Spectral Array (LEISA), a short-wavelength IR hyperspectral imager. A dichroic beamsplitter transmits IR wavelengths longer than 1.1 μm to LEISA and reflects shorter wavelengths to MVIC.

MVIC is composed of seven independent charge-coupled device (CCD) arrays on a single substrate. Six large-format (5024 × 32 pixel) CCD arrays operate in time delay integration (TDI) mode, providing two panchromatic (400 to 975 nm) channels and four color channels: BLUE (400 to 550 nm), RED (540 to 700 nm), NIR (780 to 975 nm), and narrow-band methane ("CH4," 860 to 910 nm; the 4 in the filter name is full-size to distinguish it from the chemical formula). Using TDI allows very-large-format images to be obtained as the spacecraft scans the field of view (FOV) rapidly across the scene. A single MVIC pixel is 20 μrad × 20 μrad, resulting in a total FOV of 5.7° in the direction orthogonal to the scan. This width is well matched to the size of Pluto as seen from New

[1]Lowell Observatory, Flagstaff, AZ 86001, USA. [2]Massachusetts Institute of Technology, Cambridge, MA 02139, USA. [3]NASA Jet Propulsion Laboratory, La Cañada Flintridge, CA 91011, USA. [4]Southwest Research Institute, Boulder, CO 80302, USA. [5]NASA Ames Research Center, Space Science Division, Moffett Field, CA 94035, USA. [6]Carl Sagan Center, SETI Institute, Mountain View, CA 94043, USA. [7]NASA Goddard Space Flight Center, Greenbelt, MD 20771, USA. [8]Université Grenoble Alpes, CNRS, IPAG, F-38000 Grenoble, France. [9]Department of Astronomy, University of Maryland, College Park, MD 20742, USA. [10]Department of Astronomy, University of Virginia, Charlottesville, VA 22904, USA. [11]Johns Hopkins University Applied Physics Laboratory, Laurel, MD 20723, USA. [12]Stanford University, Stanford, CA 94305, USA. [13]Lunar and Planetary Institute, Houston, TX 77058, USA. [14]Space Telescope Science Institute, Baltimore, MD, USA. [15]Planetary Science Institute, Mumbai, India. [16]Southwest Research Institute, San Antonio, TX 28510, USA.
*Corresponding author. E-mail: w.grundy@lowell.edu

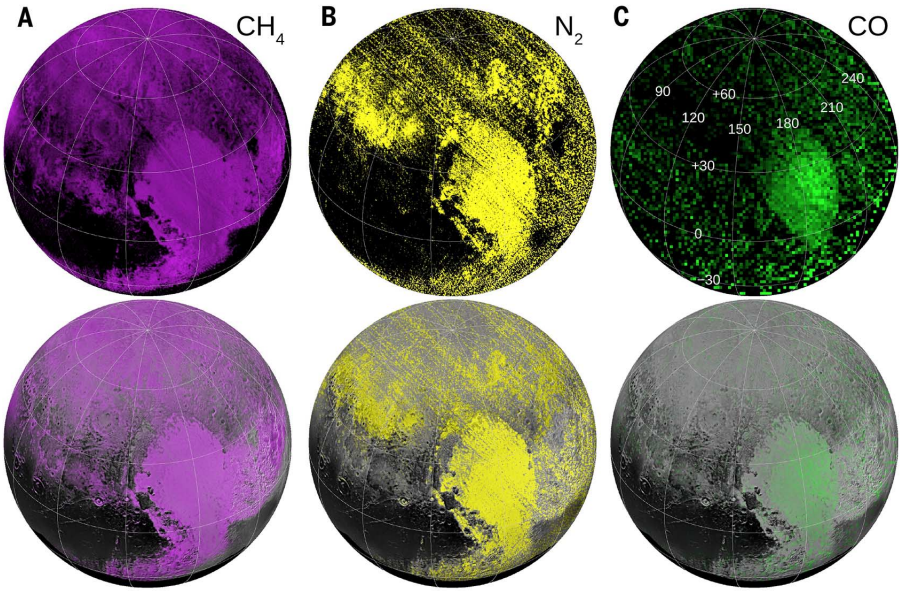

Fig. 1. LEISA maps of Pluto's volatile ices CH_4, N_2, and CO. For each species, the top panel shows the LEISA map, with brighter colors corresponding to greater absorption; the bottom panel shows the same data overlaid on a base map made from LORRI images reprojected to the geometry of the LEISA observation. (**A**) The CH_4 absorption map shows the equivalent width of the 1.3- to 1.4-μm band complex. (**B**) The N_2 absorption map is a ratio of the average over the band center (2.14 to 2.16 μm) to that of adjacent wavelengths (2.12 to 2.14 μm and 2.16 to 2.18 μm). (**C**) The CO absorption map is a ratio of the average over the band center (1.56 to 1.58 μm) to that of adjacent wavelengths (1.55 to 1.56 μm and 1.58 to 1.59 μm). Latitude and longitude grids at 30° intervals [shown in (C)] apply to all maps.

Horizons near closest approach. The seventh CCD is a 5024 × 128 element frame transfer panchromatic array operated in staring mode, with a FOV of 5.7° × 0.15°.

LEISA produces spectral maps in the compositionally important 1.25- to 2.5-μm IR spectral region by imaging a scene through a wedged etalon filter (*9*) mounted above a 256 × 256 pixel mercury cadmium telluride (HgCdTe) detector array with 62 μrad × 62 μrad pixels. LEISA forms a spectral map by scanning the 0.91° × 0.91° FOV across the scene in a push-broom fashion. The filter was fabricated such that the wavelength varies along the scan direction. It has two segments: (i) 1.25 to 2.5 μm with an average spectral resolving power of 240, and (ii) 2.1 to 2.25 μm with an average spectral resolving power of 560.

Supporting observations were obtained with the Long Range Reconnaissance Imager (LORRI) (*10*). LORRI's 1024 × 1024 pixel CCD detector has no filter, providing panchromatic response from 350- to 850-nm wavelengths, with a 608-nm pivot wavelength [a measure of effective wavelength independent of the source spectrum (*11*)]. It provides a narrow FOV (0.29°) and high spatial resolution (4.95-μrad pixels). In this paper, the LORRI images are used to provide high-resolution geological context imagery and to derive the absolute reflectance of the surface.

Pluto

New Horizons scanned the LEISA imaging spectrometer across the planet several times on the closest approach date, 14 July 2015. We present two LEISA scans, obtained at 9:33 and 9:48 UTC from ranges of 114,000 km and 102,000 km (*12*). The resulting spatial scales are 7 km per pixel and 6 km per pixel, respectively. In combination, the two observations cover the visible disk of Pluto. The data are used to map absorption by various molecules across Pluto's surface, including methane (CH_4), nitrogen (N_2), carbon monoxide (CO), and water (H_2O) ices, revealing that these ices have complex and distinct spatial distributions as described below.

Pluto's volatile ices

N_2, CO, and CH_4 ices are all volatile at Pluto's surface temperatures of 35 to 50 K (*13*, *14*). They support Pluto's atmosphere via vapor pressure equilibrium and participate in Pluto's seasonal cycles (*15*). Of the three, N_2 has the highest vapor pressure and thus dominates the lower atmosphere, while CH_4 is the least volatile, with a vapor pressure one-thousandth that of N_2 (*13*). N_2, CO, and CH_4 ices are all soluble in one another to varying degrees, so on Pluto's surface, the three ices are likely mixed to some extent at the molecular level (*16*–*18*). The volatility contrasts and complex thermodynamic behaviors of ice mixtures are expected to produce distinct spatial distributions of these ices across Pluto's surface as functions of season, heliocentric distance, latitude, altitude, local slope, substrate albedo, and thermal properties. The LEISA data reveal complex distributions of the volatile ices (Fig. 1). Brighter colors correspond to greater absorption by each ice, but the scale is arbitrary, so only relative variations are meaningful in this context. The geological context is shown by overlaying each colored absorption map on the higher-resolution LORRI base map (*4*) in the bottom part of each panel.

CH_4 ice's numerous absorption bands dominate Pluto's NIR spectrum. Figure 1A shows absorption by CH_4 ice at 1.3 to 1.4 μm to be widely distributed across the planet's surface. The CH_4 absorption is especially strong in the bright, heart-shaped region informally known (*19*) as Tombaugh Regio (TR), in Tartarus Dorsa to the east, in the high northern latitudes of Lowell Regio, and in the sliver of the southern winter hemisphere visible south of Cthulhu Regio. CH_4 absorption appears relatively uniform across the 1000-km-wide icy plain of Sputnik Planum (SP), the western half of TR. At northern mid-latitudes, the CH_4 distribution is much more patchy, evidently influenced by topographic features (see fig. S4). Many craters show strong CH_4 absorption on their rims but not on their floors, although there is some variability to this pattern. Figure 1A shows the floors of Burney and Kowal craters having some CH_4 absorption, whereas those of Giclas and Drake craters look more depleted (see also fig. S4). In eastern TR, the region around Pulfrich crater has conspicuously little CH_4 absorption. Other areas with weak CH_4 absorption include parts of al-Idrisi and Baré Montes west of SP and the low-albedo equatorial regions Cthulhu Regio and Krun Macula, although a few crater rims and the peaks of a mountainous ridge within Cthulhu Regio do show strong CH_4 absorption.

N_2 ice was first identified on Pluto from its weak absorption band at 2.15 μm (*20*). The absorption coefficient of this band is less than that of CH_4 at similar wavelengths by a factor of ~10^5, so the fact that it could be detected at all suggests that N_2 could be the dominant ice on the surface of the planet. Figure 1B shows a map of N_2 ice absorption from LEISA data. Relatively little absorption is seen at low latitudes, except for SP, where N_2 absorption is strong. As with the CH_4 absorption, N_2 absorption is patchy in northern mid-latitudes, but the spatial distribution is quite distinct from that of CH_4. N_2 absorption appears strongest on many crater floors, notably those of Burney, Safronov, Kowal, and Drake craters, consistent with topographic control (Fig. 1B and fig. S4). Little N_2 absorption is seen in Lowell Regio, possibly related to seasonal sublimation because high northern latitudes have been exposed to continuous sunlight since the late 1980s (*21*). However, substantial path lengths are required to produce observable N_2 absorption [e.g., (*20*, *22*)], so lack of absorption does not necessarily exclude its presence. A texture that produces short optical path lengths through the N_2 ice could also make it undetectable.

CO ice has absorption bands at 1.58 and 2.35 μm (*20*, *22*). Because the 2.35-μm CO band is entangled with adjacent strong CH_4 bands, we constructed a CO map using the more isolated 1.58-μm band. This band is very narrow and shallow, producing a noisy map; to help overcome the noise, it was spatially binned to 24 km × 24 km pixels. The most salient feature in the CO map (Fig. 1C) is greater absorption in SP, most prominently to the south of ~40°N latitude.

SP stands out as the one region of Pluto's encounter hemisphere where all three volatile ices coexist. This region has been interpreted as a cold trap where volatile ices have accumulated in a topographic low, possibly originating as an impact basin (*4*). The uncratered and therefore young surface of SP is apparently refreshed by glacial flow of volatile ices, possibly driven by convective overturning (*4*). The absorptions of Pluto's two most volatile ices, N_2 and CO, are especially prominent south and east of a line running roughly from Zheng-He Montes to the southern part of Cousteau Rupes. The greater absorption by N_2 and CO ices in the core of SP coincides with higher albedos and possibly elevations, perhaps indicating the area of most active or recent convective recycling.

Pluto's less volatile surface materials

Water ice, heavier hydrocarbons, and other materials had long been sought on Pluto. Absorptions of H_2O and CO_2 ices are readily apparent in the spectra of Neptune's largest moon Triton (*23*–*25*), considered an analog for Pluto. Pluto's stronger CH_4 absorptions frustrated the unambiguous detection of H_2O from Earth-based observations [e.g., (*26*)]. CO_2 ice's narrow absorptions have never been reported in remote observations of Pluto, and New Horizons LEISA observations have produced no unambiguous detection of exposed CO_2 ice.

LORRI images of Pluto show mountain ranges bordering SP (*3*, *4*). These mountains, some as high as several kilometers, could not be constructed of the volatile ices N_2, CH_4, and CO and still endure for geological time scales (*27*, *28*). H_2O ice is the most cosmochemically abundant durable material consistent with Pluto's origins and likely internal structure [e.g., (*29*)].

The broad nature of H_2O ice absorption bands and the plethora of strong CH_4 bands make mapping Pluto's H_2O with simple ratios or equivalent widths difficult. Instead, we computed the linear correlation coefficient with an H_2O ice template spectrum (Fig. 2). The highest correlations are in the vicinity of Pulfrich crater in east TR, and also along Virgil Fossa. In MVIC enhanced color images, the water-rich region in Virgil Fossa appears distinctly reddish-orange in color (see below). High H_2O spectral correlations are seen in several regions in Viking Terra and Baré Montes, with similarly reddish-orange coloration in the enhanced MVIC color images. In contrast, the H_2O-rich region around Pulfrich crater looks more neutral in the color images. Other montes including al-Idrisi, Hillary, and Zheng-He have lower correlation values, but when their spectra are compared with more CH_4-dominated spectra such as "a" and "e," they show clear evidence for water ice via enhanced absorption at 1.5 and 2.0 μm (Fig. 3 and fig. S5). Localized H_2O-rich regions in these areas tend to correspond to valleys between individual mountain peaks or topographic lows, as in the core of al-Idrisi Montes, rather than the summits of the mountains.

Cthulhu Regio shows some correlation with the water ice template spectrum, especially toward the west and along the northern and southern flanks of the regio, but Cthulhu's H_2O absorptions at 1.5 and 2.0 μm are relatively shallow. An absorption around 2.3 μm is probably indicative of hydrocarbons heavier than CH_4. The occurrence of heavier hydrocarbons in Cthulhu Regio is consistent with ground-based observations suggesting that ethane ice absorptions are most prominent at those longitudes (*30*), although additional hydrocarbons are also likely to be contributing to the absorption in that wavelength region. A region toward the east of Cthulhu, near the equator, shows little evidence of H_2O absorption and could represent the spot richest in tholins across Pluto's encounter hemisphere.

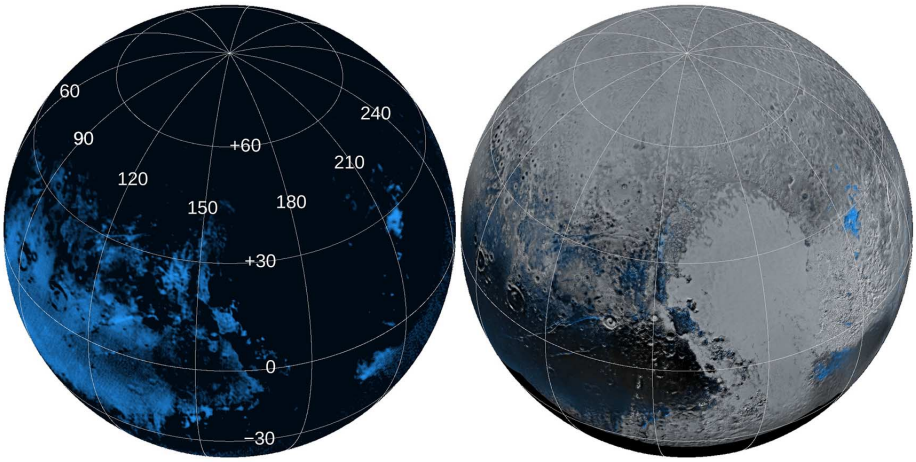

Fig. 2. LEISA map of Pluto's nonvolatile H_2O ice. Left: Map showing the correlation coefficient between each LEISA spectrum and a template Charon-like H_2O ice spectrum [e.g., (47, 49)], highlighting where H_2O absorption is least contaminated by other spectral features. Right: LEISA map superposed on the reprojected LORRI base map.

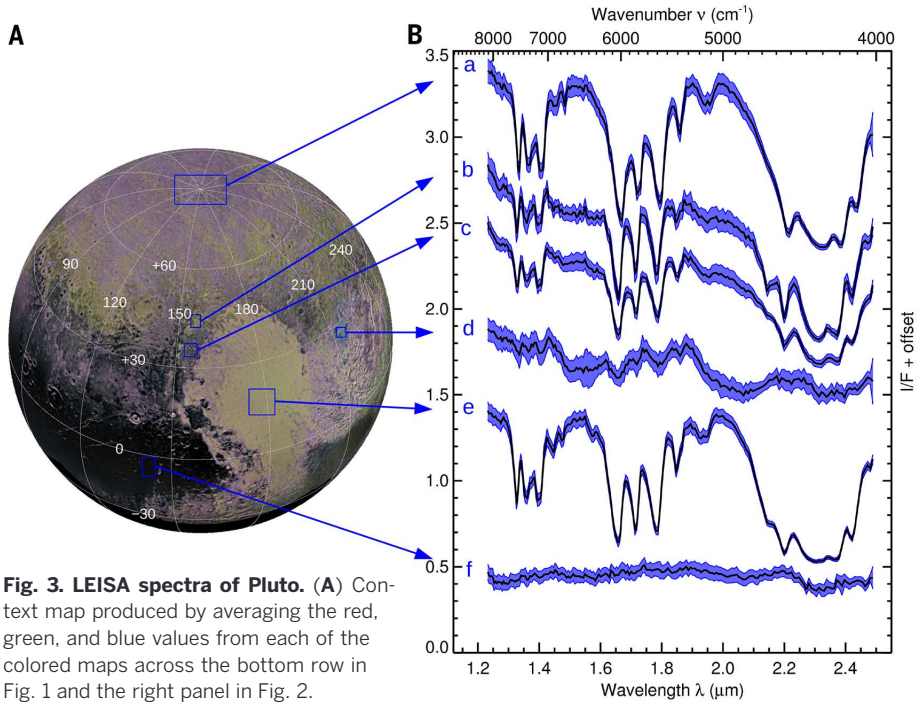

Fig. 3. LEISA spectra of Pluto. (**A**) Context map produced by averaging the red, green, and blue values from each of the colored maps across the bottom row in Fig. 1 and the right panel in Fig. 2. (**B**) Specific intensity (I/F) spectra averaged over regions in blue boxes, with envelopes indicating the standard deviations within the boxes. These regions were selected to highlight Pluto's spectral diversity. Vertical offsets for spectra "a" through "f" are +2.3, +1.7, +1.5, +1.2, +0.45, and 0, respectively. Pluto's north pole ("a") shows strong absorptions by CH_4 ice. Spectrum "b" is a region characterized by a strong N_2 ice absorption at 2.15 μm and weak H_2O ice bands at 1.5 and 2 μm. Spectrum "c" is al-Idrisi Montes, very similar to "b" except without the N_2 absorption. The area around Pulfrich crater ("d") has H_2O ice absorptions at 1.5, 1.65, and 2 μm and comparatively weak CH_4 ice absorptions. Spectrum "e" is the center of Sputnik Planum, with strong CH_4 bands, N_2 ice absorption at 2.15 μm, and CO ice absorption at 1.58 μm. Spectrum "f" is eastern Cthulhu Regio, with weak H_2O ice absorptions at 1.5 and 2 μm and a feature attributed to heavier hydrocarbons at 2.3 μm.

Pluto colors

MVIC obtained color images of Pluto on multiple epochs. We present an observation obtained on 14 July 2015, 11:11 UTC, about 40 min prior to closest approach, from a range of 35,000 km. The resulting spatial scale was 700 m per pixel, the best color spatial resolution returned to Earth thus far. Figure 4A shows an "extended" color view of this data set, in which MVIC's BLUE, RED, and NIR filter images are displayed in the blue, green, and red channels, respectively.

Color ratios remove illumination effects and highlight color variability, as shown in Fig. 4B. RED/BLUE and NIR/RED ratios both vary by more than a factor of 2 across Pluto's encounter hemisphere. Most of this variation is distributed along an axis from blue/neutral colors in the lower left to much redder colors in the upper right, but various clumps and deviations from this axis are indicative of additional subtleties.

Pluto's color diversity is further explored via principal components analysis (PCA), projecting brightnesses in the four MVIC filters into an orthogonal basis set where each dimension successively accounts for the maximum amount of remaining variance. The first principal component (PC1) corresponds to overall brightness across the scene. PC1 accounts for 98.8% of the variance of the MVIC color data, mostly due to illumination geometry and to Pluto's extreme albedo variations (see below). Principal components 2, 3, and 4 account for 1%, 0.12%, and 0.05% of the total variance in the full MVIC data set, respectively. The coherent spatial patterns seen in all three are indicative of distinctly colored provinces across Pluto's surface. Shown in Fig. 4, C to F, are the four principal component images along with the eigenvectors; Fig. 4G combines the principal component images, showing many distinct color units.

We used the narrow MVIC CH4 filter in conjunction with RED and NIR filters to compute a CH_4 equivalent-width map (Fig. 5) and a color slope map (fig. S3; details in supplementary text). A key distinction between this and the LEISA CH_4 map in Fig. 1 is that they probe two different CH_4 ice bands. The 0.89-μm band targeted by the MVIC CH4 filter has a peak absorption coefficient roughly an order of magnitude below that of the 1.3- to 1.4-μm band complex being mapped in Fig. 1 (*31*). Consequently, Fig. 5 is mapping greater path lengths in CH_4 ice, and thus areas that are especially rich in CH_4 ice and/or have especially large particle sizes. The distribution is broadly similar to the LEISA CH_4 map, but there are differences. Regions standing out for their strong 0.89-μm band absorption include the bladed terrain of Tartarus Dorsa and low-latitude bands flanking Cthulhu Regio. The much higher spatial resolution of the MVIC observation makes it

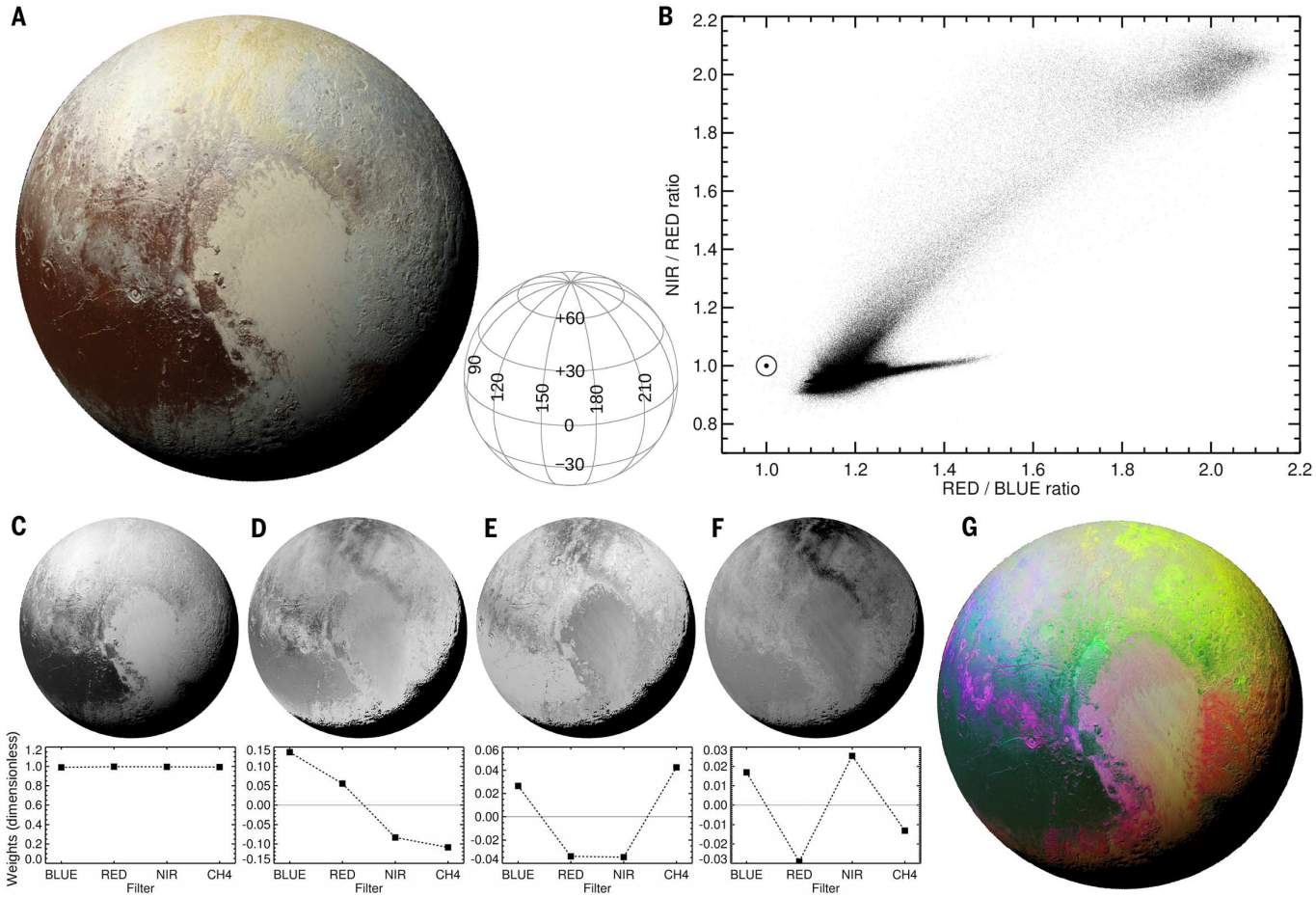

Fig. 4. MVIC colors of Pluto. (**A**) "Enhanced" color with MVIC's BLUE, RED, and NIR filter images displayed in blue, green, and red color channels, respectively. Geometry is indicated by the wire grid. (**B**) Distribution of NIR/RED and RED/BLUE color ratios, excluding regions where the incidence angle from the Sun or the emission angle to the spacecraft exceeds 70° from the zenith. The Sun symbol indicates neutral colors; redder colors extend up and to the right. (**C** to **F**) Principal component images and eigenvectors for PC1 to PC4, respectively. (**G**) False-color view with shading from PC1 and the hue set by PC2, PC3, and PC4 displayed in red, green, and blue channels, respectively.

possible to see subtle variations in CH_4 absorption within SP. The north, west, and southwest margins of SP show stronger CH_4 absorption. In the core of SP, where absorptions of the more volatile ices N_2 and CO are more prominent, the boundaries between the polygonal convection cells [described in (*1*, *4*)] show less CH_4 absorption.

When Pluto's known atmospheric gases (N_2, CH_4, and CO) are exposed to energetic photons or charged particles, chemical reactions produce more complex radicals and molecules that are generally nonvolatile at Pluto's surface temperatures (*32*–*34*). Similar photolytic and radiolytic processing occurs in these same molecules condensed as ices (*35*, *36*). Pluto's present-day atmosphere is opaque to Lyman-alpha (Ly-α) solar ultraviolet light (*21*), so photochemical products are mostly produced in the atmosphere, condense as haze particles, and eventually settle to the surface. Because in the present epoch Ly-α does not reach the surface, ices on the surface are currently primarily affected by interstellar pickup ions, galactic rays, and their spallation products from their interactions with the atmosphere. Cosmic rays can induce chemical changes at depths exceeding 1 m into the surface (*37*, *38*).

Laboratory simulations of radiolysis of a Pluto ice mixture at $T \approx 15$ K (*39*) yield refractory residues with colors resembling some of the colors on Pluto. Chemical analysis of this material shows atomic ratios N/C ≈ 0.9 and O/C ≈ 0.2, indicating that the 1.2-keV electrons used in the experiments dissociate the N_2 molecule, allowing the N atoms to react with other atoms and molecular fragments. The residue contains urea, alcohols, carboxylic acids, ketones, aldehydes, amines, and nitriles. A substantial aromatic component is found in two-step laser desorption mass spectroscopy, with mass peaks throughout the range ~50 to 250 daltons.

During any putative epoch when Pluto's atmosphere collapses, it would not shield the surface from ultraviolet photons and solar wind particles as it does now. These would then reach the surface and directly contribute to its chemical evolution. The production of the colored ice residue in the laboratory with low-energy electrons occurs in a matter of hours with an electron fluence of ~10^{17}/mm^2. Charged particles and scattered Ly-α can arrive from all directions, so in the absence of an atmosphere, coloration could arise as quickly as a few years, even on unilluminated surface regions, much faster than the ~40,000-year time scale for tholin haze deposition from Pluto's atmosphere (*5*).

Pluto albedos

Four major global albedo units are evident in New Horizons Pluto images: low-albedo equatorial regions exemplified by Cthulhu Regio and Krun Macula, the northern summer polar region Lowell Regio, a sliver of southern winter hemisphere, and the high-albedo TR. TR's albedo is similar to that of Triton (*40*). Pluto's dark equatorial regions have albedos similar to some outer solar system moons that are rich in carbonaceous or organic material, such as the saturnian moons Hyperion and Phoebe and the uranian moon Umbriel, although they are not as dark as the low-albedo hemisphere of Iapetus (*41*).

In planetary surface images, intensity differences are mostly due to illumination and observing geometry. A photometric function is needed to obtain quantitative measurements of normal albedo (brightness for incident, emission, and

solar phase angles all equal to 0°). Figure 6A is a global map of normal albedo from LORRI images, using a photometric function in which 30% of the reflected photons obey Lambertian scattering while the rest follow a single-scattering lunar function (see supplementary text). This function is similar to those found for the icy moons of Saturn (*41*). We also accounted for the 0.04 magnitude opposition surge shown in Fig. 6C for phase angles below 0.10° (*42*, *43*).

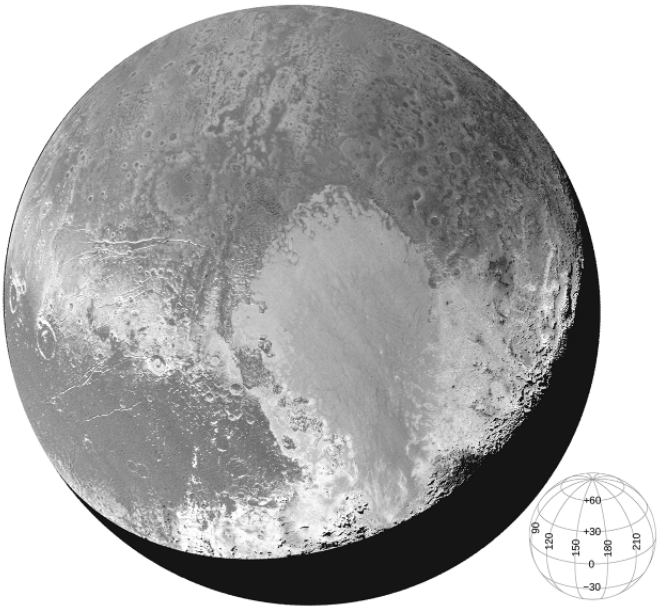

Fig. 5. Pluto MVIC CH_4 absorption map. The equivalent width of absorption in the MVIC CH4 filter is computed by comparison with the NIR and RED filter images (see supplementary text for details). This filter is centered on a weaker CH_4 ice absorption than the one mapped with LEISA data in Fig. 1. Brighter shades correspond to stronger CH_4 ice absorption. Differences between the maps are discussed in the text. Except for a sliver of poorly illuminated terrain along the terminator, where geometric effects become extreme, most of the contrast in this map corresponds to regional variations in CH_4 ice absorption.

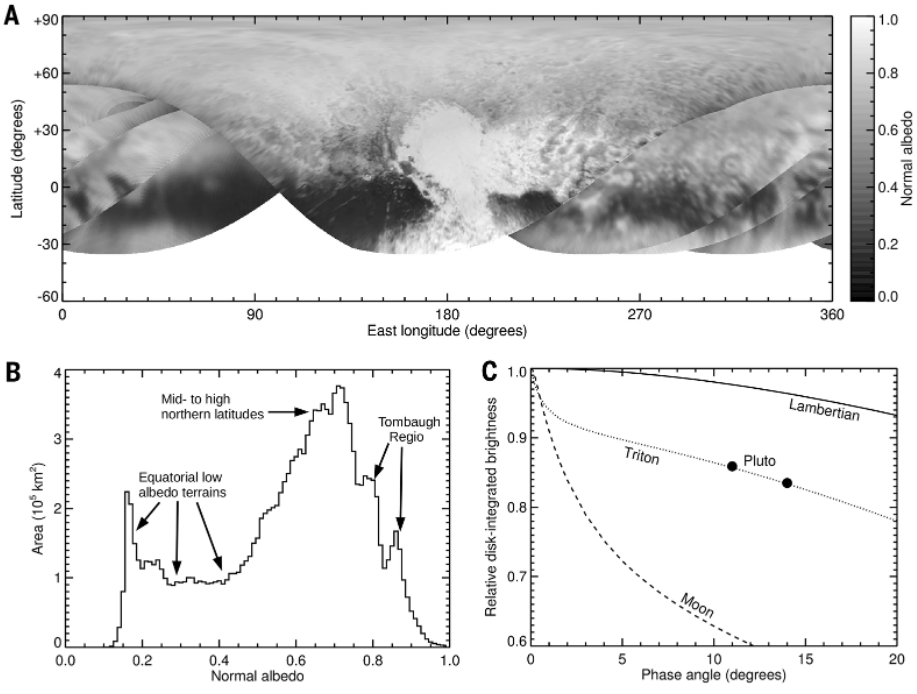

Fig. 6. LORRI albedos on Pluto. (**A**) Normal albedo across Pluto from LORRI panchromatic images sensitive to wavelengths from 350 to 850 nm (*10*). (**B**) Histogram of albedo values. (**C**) Decline of Pluto's disk-integrated brightness with phase angle, compared with the same data for a Lambertian sphere, the icy satellite Triton, and Earth's Moon. The Triton curve is based on Voyager green filter and ground-based observations with an effective wavelength of 550 nm (*40*). The lunar curve is for a Johnson V filter wavelength of 550 nm. The Pluto data points show LORRI brightness after correcting for light-curve variability, relative to zero-phase data from ground-based monitoring (*43*) (Bessel R filter, 630 nm).

This albedo map illustrates the quantitative differences in albedo for regions characterized by the distinct combinations of volatile ices and colors seen in the preceding figures. Albedo and composition can interact in complex ways: High-albedo regions that absorb less sunlight tend to become sites of volatile ice deposition, whereas low-albedo regions can absorb much more sunlight, driving sublimation of volatiles and reaching higher temperatures. Deposition of volatile ices can raise the albedos of regions if they are configured into textures that scatter light, and the texture of mixed volatile ices can change as a result of annealing, sintering, or temperature changes that lead to phase transitions or fracturing.

Charon

Charon colors

Figure 7A shows the highest–spatial resolution MVIC color observation of Charon from New Horizons, with a spatial scale of 1.5 km per pixel. The spacecraft recorded this scan on 14 July 2015, 10:42 UTC, about 70 min before closest approach, from a range of 74,000 km. As previously known from Earth-based observations, Charon's surface color is generally neutral (*44*, *45*). New Horizons data reveal a large-scale exception with Mordor Macula, the northern polar region, being distinctly red. The red coloration begins to appear northward of about 45°, as measured by NIR/BLUE and NIR/RED color ratios (Fig. 7B). In addition to this large-scale feature, there are a variety of local color variations. Craters and other features complicate or interrupt the trend toward redder coloration at high latitudes, such as Dorothy Gale crater, which is less red than the local latitude trend, and Vader crater, which is more red. Lower-latitude color variations include the ejecta of Nasreddin crater being bluer than surrounding terrain, and Gallifrey Macula redder. North and south of the tectonic belt extending across Charon's encounter hemisphere, colors are similar, but the smoother plains of Vulcan Planum show less color diversity.

Charon MVIC color ratios (Fig. 7C) show a simpler distribution of colors than seen on Pluto. The bulk of the surface is spectrally neutral, with a mixing trend toward the redder colors at high latitudes. Principal components analysis of the four colors corroborates this simple color distribution. As before, PC1 (Fig. 7D) maps brightness across the scene, controlled by albedo and illumination geometry, accounting for 97.3% of the observed variance. PC2 corresponds to the reddish polar coloration (Fig. 7E), albeit inverted so the pole looks dark. It accounts for 2.7% of the observed variance, greater than for Pluto's PC2. Charon's PC3 and PC4 show little coherent structure (Fig. 7, F and G), apparently responding primarily to noise. They account for only 0.03% and 0.02%, respectively, of the variance—much less than their counterparts on Pluto.

Charon spectral characteristics

New Horizons observed Charon with LEISA from a range of 82,000 km on 14 July 2015, 10:30 UTC, at a spatial scale of 5 km per pixel. The data

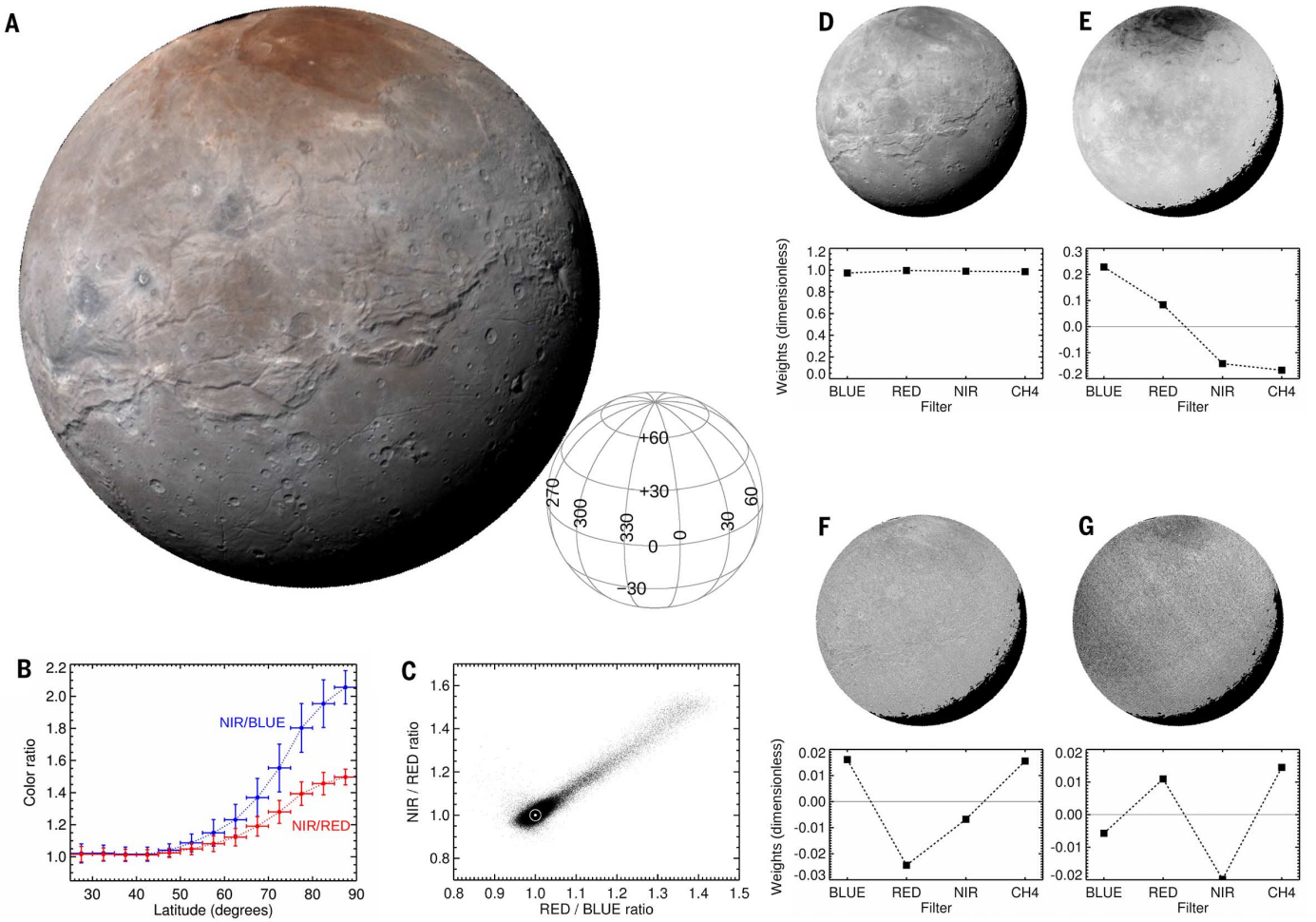

Fig. 7. MVIC colors of Charon. (**A**) Enhanced color, with MVIC's BLUE, RED, and NIR filter images displayed in blue, green, and red color channels, respectively. Geometry is indicated by the associated wire grid. (**B**) MVIC NIR/BLUE and NIR/RED color ratio means and standard deviations averaged over 5° latitude annuli, excluding points near the limb with emission angles greater than 75°. (**C**) Scatterplot of NIR/RED and RED/BLUE color ratios, excluding incidence and emission angles greater than 70°. Most pixels cluster near solar colors, with a mixing line extending toward redder colors at upper right. (**D** to **G**) Principal component images and eigenvectors for principal components 1, 2, 3, and 4, respectively.

confirm that Charon's encounter hemisphere is composed predominantly of water ice, as first identified in the mid-1980s (*46*). Earth-based observations had also shown that Charon's water ice was at least partially in the crystalline phase, as indicated by the 1.65-μm band, and that the water absorption was seen at all longitudes as Charon rotated (*47*–*49*). LEISA observations confirm that water ice is everywhere on Charon's encounter hemisphere, with the 1.5-, 1.65-, and 2-μm bands being evident in all of the example spectra in Fig. 8.

Spectral observations also revealed an absorption band around 2.22 μm, attributed to ammonia hydrates (*47*–*49*). Subsequent studies (*50*, *51*) showed that the band varies with sub-observer longitude as Charon rotates. LEISA observations now show that the ammonia absorption is distributed across Charon's encounter hemisphere at a low level, with local concentrations associated with a few of Charon's bright rayed craters. Organa crater in the northern hemisphere is the best example. The crater is about 5 km across and is thus not resolved by the LEISA pixels. The NH_3 signature appears to be associated with the crater plus some, but not all, of the ejecta blanket (see Fig. 8C and fig. S6). According to laboratory studies, ammonia ice is destroyed by ultraviolet photons and cosmic rays (*52*, *53*). From fluxes in Charon's environment (*38*), the time scale for radiolytic destruction of Charon's NH_3 was estimated to be on the order of 10^7 years (*50*), implying that these deposits are relatively recent.

LEISA spectra of Mordor Macula do not reveal distinguishing spectral features coinciding with the red coloration, apart from subtle differences in continuum slope toward the shorter-wavelength end of LEISA's spectral range. The reddish colorant may be too thin to produce stronger features at NIR wavelengths, or may simply lack distinct absorption bands at LEISA wavelengths.

Discussion

Various patterns emerge from the observations. Latitude-dependent distributions of materials were expected from seasonal volatile transport processes (*54*), and indeed, the LEISA and MVIC data confirm a number of distinct latitude zones, especially in the western half of the encounter hemisphere. Pluto's equatorial latitudes feature regions that are strikingly dark and red at visible wavelengths, typified on the encounter hemisphere by Cthulhu Regio and Krun Macula. These provinces are much less dark at IR wavelengths, and in many areas they show weak 1.5- and 2-μm features of H_2O ice, along with absorptions by hydrocarbons around 2.3 μm (Fig. 3). A possible scenario is that these regions are ancient, heavily cratered landscapes where tholins and other inert materials have accumulated over geological time scales.

Flanking the dark equatorial belt to both the north and south are higher-albedo regions rich in CH_4 ice (Figs. 1A and 5). As the least volatile of Pluto's volatile ices, it should be the first to condense and the last to sublimate away, consistent with its proximity to the volatile-depleted maculae. The CH_4 is most prominent in topographically high regions such as ridges and crater rims, and CH_4 can even be found in a few isolated high-altitude regions within the maculae. The bladed

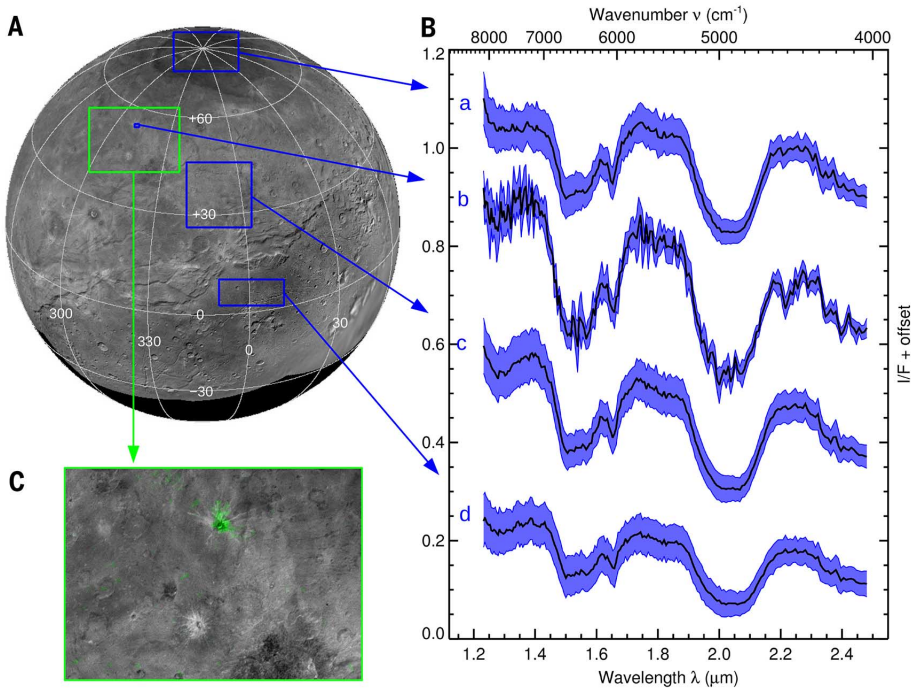

Fig. 8. LEISA spectra of Charon. (**A**) LORRI composite base map. Regions where I/F spectra were averaged for plotting in (B) are indicated by blue boxes. (**B**) Vertical offsets for spectra "a" through "d" are +0.7, +0.4, +0.2, and 0, respectively. All four spectra show the characteristic absorption bands of cold, crystalline H_2O ice at 1.5, 1.65, and 2 μm. Charon's north pole ("a") shows a little more continuum absorption toward short wavelengths, but no other obvious differences, relative to spectra from lower latitudes on Charon. Spectrum "b" is a region around Organa crater showing NH_3 absorption at 2.22 μm. (**C**) Close-up of the region indicated by the green box in (A), with 2.22-μm absorption mapped in green to show the spatial distribution of NH_3-rich material (fig. S6 shows the full map). Spectra "c" and "d" compare plains units above and below the tectonic belt.

terrain of Tartarus Dorsa is especially CH_4-rich (Figs. 1A and 5), and this could be the result of many seasonal cycles of CH_4 accumulation on elevated low-latitude regions. At northern latitudes above ~35°N, more volatile N_2 ice begins to appear, favoring topographic lows where the surface pressure is higher (Fig. 1B). Still farther north, N_2 and CO absorptions are weak in Lowell Regio (Fig. 1, B and C), whereas CH_4 absorption continues right up to the pole (Figs. 1A and 5). This high-albedo region has been described as a "polar cap," although the lack of prominent N_2 and CO ice absorptions makes that term seem poorly suited to describing a summer pole comparatively depleted in Pluto's more volatile ices.

This latitude-dependent distribution of Pluto's surface materials is interrupted in TR. The western half of TR is SP, a deep basin hosting a unique, youthful surface morphology described in detail in (*4*). The spectral signatures of N_2, CH_4, and CO ices are all present in this region, with the absorptions of the more volatile N_2 and CO ices being especially prominent in the southeastern part of SP, below the southern limit for latitudes experiencing the "midnight sun" during the current epoch (*21*). But this pattern does not seem to be purely governed by climatic factors, because the boundary curves from around Zheng-He Montes in the southwest to Columbia Colles in the northeast. Another potential explanation could involve bulk glacial flow of ices to the northwest, with ablation of the more volatile N_2 and CO from the surface of the flow. Alternatively, the locus of most active convection could migrate around within SP, with less active regions showing less absorption by the volatile ices. It is also possible to interpret the reduced volatile ice absorption toward SP's northwest flank as being due to evolution of the surface texture alone, with no change in bulk composition. A reduction in particle size or an increase in scattering could account for the reduced absorption toward that flank. Eastern TR also does not fit easily into the latitude-dependent picture described above. There appears to be a connection between the two halves, with glacial flow from east TR down into SP (*4*), and also some shared color features with wisps of CH_4-rich material with colors similar to east TR extending westward into SP (see Fig. 4G). CH_4 ice has a low density and could perhaps be transported as a crust on glacially flowing N_2 and CO ice.

Water ice presents a number of puzzles on Pluto. Its IR spectral signature is associated with two very distinct shorter-wavelength color units. H_2O-rich outcrops in Virgil Fossa and Viking Terra (Fig. 2) show a distinct, reddish color in Fig. 4A, unlike the more neutral coloration of the H_2O-rich outcrops around Pulfrich crater. Rugged mountains such as Zheng-He and Norgay Montes, which had been expected to be composed of H_2O ice, show comparatively weak H_2O spectral signatures.

Charon presents its own mysteries. The reddish polar region of Mordor Macula is a unique and striking feature not seen on other icy satellites in the outer solar system. The latitudinal dependence of its distribution suggests a mechanism involving seasonal cold trapping of volatiles such as CH_4 that would not otherwise be stable at Charon's surface. During Charon's long winter, polar latitudes remain unilluminated for multiple Earth decades, during which time they can cool to temperatures below 20 K [e.g., (*55*)]. Potential sources of CH_4 briefly resident in Charon's surface environment could be outgassing from Charon's interior and Pluto's escaping atmosphere, as discussed in (*5*, *55*). Seasonally cold-trapped CH_4 would be rapidly photolyzed by solar Ly-α radiation, roughly half of which arrives at Charon's surface indirectly via scattering by interplanetary hydrogen. Resulting radicals would combine into heavier products that are sufficiently nonvolatile to remain after Charon's pole emerges back into the sunlight and warms to summer temperatures in the 50 to 60 K range. Further photolysis and radiolysis would lead to production of reddish tholins, as discussed above. This hypothesis predicts that Charon's southern hemisphere should exhibit a similar high-latitude reddish patch.

Charon's isolated ammonia-rich areas are also intriguing. NH_3 is a potentially important geochemical material in icy satellites that has heretofore mostly eluded detection via remote sensing techniques. A possible scenario for its appearance in just a few of Charon's craters is that these impacts dredged up the NH_3 from below Charon's surface too recently for it to have been destroyed by space weathering processes. It is also possible that NH_3-rich material is delivered by a subset of impactors, or that Charon's subsurface is heterogeneous, with local subsurface concentrations of NH_3 emplaced during an earlier era of cryovolcanic activity being subsequently exhumed by impacts.

Conclusions

We have presented spatially resolved visible and near-infrared observations of the encounter hemispheres of Pluto and Charon, obtained by the New Horizons spacecraft on 14 July 2015. Data returned so far reveal complex spatial distributions of Pluto's CH_4, N_2, and CO ices as well as the local emergence of water-ice bedrock and broad expanses of accumulated tholins at low latitudes. The data point to atmospheric and geological processes having acted over a range of time scales to create the currently observed surface. On Charon, the presence and distribution of localized ammonia-ice outcrops and of reddish circumpolar material raise questions about the exogenous and endogenous processes acting on this large satellite.

Many of the data collected by New Horizons have yet to be transmitted back to Earth. They will enable us to quantitatively map the composition, state, and texture distributions of the system's inventory of materials in order to disentangle the

history of these icy bodies and understand their place in the broader context of the outer solar system.

REFERENCES AND NOTES

1. H. A. Weaver, W. C. Gibson, M. B. Tapley, L. A. Young, S. A. Stern, Overview of the New Horizons science payload. **Space Sci. Rev. 140**, 75–91 (2008). doi: 10.1007/s11214-008-9376-6
2. L. A. Young **et al.**, New Horizons: Anticipated scientific investigations at the Pluto system. **Space Sci. Rev. 140**, 93–127 (2008). doi: 10.1007/s11214-008-9462-9
3. S. A. Stern **et al.**, The Pluto system: Initial results from its exploration by New Horizons. **Science 350**, aad1815 (2015). doi: 10.1126/science.aad1815; pmid: 26472913
4. J. M. Moore **et al.**, The geology of Pluto and Charon through the eyes of New Horizons. **Science 351**, 1284–1293 (2016).
5. G. R. Gladstone **et al.**, The atmosphere of Pluto as observed by New Horizons. **Science 351**, aad8866 (2016). doi: 10.1126/science.aad8866
6. F. Bagenal **et al.**, Pluto's interaction: Solar wind, energetic particles, dust. **Science 351**, aad9045 (2016). doi: 10.1126/science.aad9045
7. H. A. Weaver **et al.**, The small satellites of Pluto as observed by New Horizons. **Science 351**, aae0030 (2016). doi: 10.1126/science.aae0030
8. D. C. Reuter **et al.**, Ralph: A visible/infrared imager for the New Horizons Pluto/Kuiper belt mission. **Space Sci. Rev. 140**, 129–154 (2008). doi: 10.1007/s11214-008-9375-7
9. K. P. Rosenberg, K. D. Hendrix, D. E. Jennings, D. C. Reuter, M. D. Jhabvala, A. T. La, Logarithmically variable infrared etalon filters. **Proc. SPIE 2262** (1994). doi: 10.1117/12.185804
10. A. F. Cheng **et al.**, Long-Range Reconnaissance Imager on New Horizons. **Space Sci. Rev. 140**, 189–215 (2008). doi: 10.1007/s11214-007-9271-6
11. A. Tokunaga, W. D. Vacca, The Mauna Kea Observatories near-infrared filter set. III. Isophotal wavelengths and absolute calibration. **Publ. Astron. Soc. Pac. 117**, 421–426 (2005). doi: 10.1086/429382
12. All ranges reported in this paper are relative to target center.
13. N. Fray, B. Schmitt, Sublimation of ices of astrophysical interest: A bibliographic review. **Planet. Space Sci. 57**, 2053–2080 (2009). doi: 10.1016/j.pss.2009.09.011
14. E. Lellouch, J. Stansberry, J. Emery, W. Grundy, D. P. Cruikshank, Thermal properties of Pluto's and Charon's surfaces from Spitzer observations. **Icarus 214**, 701–716 (2011). doi: 10.1016/j.icarus.2011.05.035
15. S. A. Stern, L. M. Trafton, On the atmospheres of objects in the Kuiper belt. In **The Solar System Beyond Neptune**, A. Barucci, H. Boehnhardt, D. Cruikshank, A. Morbidelli, Eds. (Univ. of Arizona Press, Tucson, 2009), pp. 365–380.
16. E. Quirico, B. Schmitt, Near-infrared spectroscopy of simple hydrocarbons and carbon oxides diluted in solid N_2 and as pure ices: Implications for Triton and Pluto. **Icarus 127**, 354–378 (1997). doi: 10.1006/icar.1996.5663
17. S. Douté **et al.**, Evidence for methane segregation at the surface of Pluto. **Icarus 142**, 421–444 (1999). doi: 10.1006/icar.1999.6226
18. L. A. Trafton, On the state of methane and nitrogen ice on Pluto and Triton: Implications of the binary phase diagram. **Icarus 246**, 197–205 (2015). doi: 10.1016/j.icarus.2014.05.022
19. All place names used in this paper are informal designations at this time. Maps showing them are available as figs. S1 and S2.
20. T. C. Owen **et al.**, Surface ices and the atmospheric composition of pluto. **Science 261**, 745–748 (1993). doi: 10.1126/science.261.5122.745; pmid: 17757212
21. A. M. Earle, R. P. Binzel, Pluto's insolation history: Latitudinal variations and effects on atmospheric pressure. **Icarus 250**, 405–412 (2015). doi: 10.1016/j.icarus.2014.12.028
22. W. M. Grundy, C. B. Olkin, L. A. Young, M. W. Buie, E. F. Young, Near-infrared spectral monitoring of Pluto's ices: Spatial distribution and secular evolution. **Icarus 223**, 710–721 (2013). doi: 10.1016/j.icarus.2013.01.019
23. D. P. Cruikshank **et al.**, Ices on the surface of Triton. **Science 261**, 742–745 (1993). doi: 10.1126/science.261.5122.742; pmid: 17757211
24. D. P. Cruikshank **et al.**, Water ice on Triton. **Icarus 147**, 309–316 (2000). doi: 10.1006/icar.2000.6451
25. W. M. Grundy **et al.**, Near-infrared spectral monitoring of Triton with IRTF/SpeX II: Spatial distribution and evolution of ices. **Icarus 205**, 594–604 (2010). doi: 10.1016/j.icarus.2009.08.005
26. W. M. Grundy, M. W. Buie, Spatial and compositional constraints on non-ice components and H_2O on Pluto's surface. **Icarus 157**, 128–138 (2002). doi: 10.1006/icar.2002.6833
27. Y. Yamashita, M. Kato, M. Arakawa, Experimental study on the rheological properties of polycrystalline solid nitrogen and methane: Implications for tectonic processes on Triton. **Icarus 207**, 972–977 (2010). doi: 10.1016/j.icarus.2009.11.032
28. S. A. Stern, S. B. Porter, A. M. Zangari, On the roles of escape erosion and the viscous relaxation of craters on Pluto. **Icarus 250**, 287–293 (2015). doi: 10.1016/j.icarus.2014.12.006
29. W. B. McKinnon, D. Prialnik, S. A. Stern, A. Coradini, Structure and evolution of Kuiper belt objects and dwarf planets. In **The Solar System Beyond Neptune**, A. Barucci, H. Boehnhardt, D. Cruikshank, A. Morbidelli, Eds. (Univ. of Arizona Press, Tucson, 2009), pp. 213–241.
30. B. J. Holler, L. A. Young, W. M. Grundy, C. B. Olkin, J. C. Cook, Evidence for longitudinal variability of ethane ice on the surface of Pluto. **Icarus 243**, 104–110 (2014). doi: 10.1016/j.icarus.2014.09.013
31. W. M. Grundy, B. Schmitt, E. Quirico, The temperature-dependent spectrum of methane ice I between 0.7 and 5 μm and opportunities for near-infrared remote thermometry. **Icarus 155**, 486–496 (2002). doi: 10.1006/icar.2001.6726
32. Y.-J. Wu, H.-F. Chen, S.-J. Chuang, T.-P. Huang, Ultraviolet and infrared spectra of electron-bombarded solid nitrogen and methane diluted in solid nitrogen. **Astrophys. J. 768**, 83 (2013). doi: 10.1088/0004-637X/768/1/83
33. Y.-J. Wu **et al.**, Spectra and photolysis of pure nitrogen and methane dispersed in solid nitrogen with vacuum-ultraviolet light. **Astrophys. J. 746**, 175 (2012). doi: 10.1088/0004-637X/746/2/175
34. Y. S. Kim, R. I. Kaiser, Electron irradiation of Kuiper belt surface ices: Ternary N_2-CH_4-CO mixtures as a case study. **Astrophys. J. 758**, 37 (2012). doi: 10.1088/0004-637X/758/1/37
35. M. H. Moore, R. L. Hudson, Infrared study of ion-irradiated N_2-dominated ices relevant to Triton and Pluto: Formation of HCN and HNC. **Icarus 161**, 486–500 (2003). doi: 10.1016/S0019-1035(02)00037-4
36. C. K. Materese **et al.**, Ice chemistry on outer solar system bodies: Carboxylic acids, nitriles, and urea detected in refractory residues produced from the UV photolysis of N_2:CH_4:CO-containing ices. **Astrophys. J. 788**, 111 (2014). doi: 10.1088/0004-637X/788/2/111
37. R. E. Johnson, Effect of irradiation on the surface of Pluto. **Geophys. Res. Lett. 16**, 1233–1236 (1989). doi: 10.1029/GL016i011p01233
38. J. F. Cooper, E. R. Christian, J. D. Richardson, C. Wang, Proton irradiation of centaur, Kuiper belt, and Oort cloud objects at plasma to cosmic ray energy. **Earth Moon Planets 92**, 261–277 (2003). doi: 10.1023/B:MOON.0000031944.41883.80
39. C. K. Materese, D. P. Cruikshank, S. A. Sandford, H. Imanaka, M. Nuevo, Ice chemistry on outer solar system bodies: Electron radiolysis of N_2-, CH_4-, and CO-containing ices. **Astrophys. J. 812**, 150 (2015). doi: 10.1088/0004-637X/812/2/150
40. B. J. Buratti **et al.**, Photometry of Triton 1992–2004: Surface volatile transport and discovery of a remarkable opposition surge. **Icarus 212**, 835–846 (2011). doi: 10.1016/j.icarus.2011.01.012
41. B. J. Buratti, Voyager disk resolved photometry of the Saturnian satellites. **Icarus 59**, 392–405 (1984). doi: 10.1016/0019-1035(84)90109-X
42. M. W. Buie, W. M. Grundy, E. F. Young, L. A. Young, S. A. Stern, Pluto and Charon with the Hubble Space Telescope II. Resolving changes on Pluto's surface and a map for Charon. **Astron. J. 139**, 1128–1143 (2010). doi: 10.1088/0004-6256/139/3/1128
43. B.J. Buratti **et al.**, Photometry of Pluto 2008-2014: Evidence of ongoing seasonal volatile transport and activity. **Astrophys. J. 804**, L6 (2015). doi: 10.1088/2041-8205/804/1/L6
44. R. P. Binzel, Hemispherical color differences on Pluto and Charon. **Science 241**, 1070–1072 (1988). doi: 10.1126/science.241.4869.1070; pmid: 17747488
45. U. Fink, M. A. DiSanti, The separate spectra of Pluto and its satellite Charon. **Astron. J. 95**, 229–236 (1988). doi: 10.1086/114632
46. M. W. Buie, D. P. Cruikshank, L. A. Lebofsky, E. F. Tedesco, Water frost on Charon. **Nature 329**, 522–523 (1987). doi: 10.1038/329522a0
47. M. E. Brown, W. M. Calvin, Evidence for crystalline water and ammonia ices on Pluto's satellite charon. **Science 287**, 107–109 (2000). doi: 10.1126/science.287.5450.107; pmid: 10615040
48. M. W. Buie, W. M. Grundy, The distribution and physical state of H_2O on Charon. **Icarus 148**, 324–339 (2000). doi: 10.1006/icar.2000.6509
49. C. Dumas, R. J. Terrile, R. H. Brown, G. Schneider, B. A. Smith, Hubble Space Telescope NICMOS spectroscopy of Charon's leading and trailing hemispheres. **Astron. J. 121**, 1163–1170 (2001). doi: 10.1086/318747
50. J. C. Cook, S. J. Desch, T. L. Roush, C. A. Trujillo, T. R. Geballe, Near-infrared spectroscopy of Charon: Possible evidence for cryovolcanism on Kuiper belt objects. **Astrophys. J. 663**, 1406–1419 (2007). doi: 10.1086/518222
51. F. E. DeMeo **et al.**, Spectral variability of Charon's 2.21-μm feature. **Icarus 246**, 213–219 (2015). doi: 10.1016/j.icarus.2014.04.010
52. G. Strazzulla, M. E. Palumbo, Evolution of icy surfaces: An experimental approach. **Planet. Space Sci. 46**, 1339–1348 (1998). doi: 10.1016/S0032-0633(97)00210-9
53. S. Pilling **et al.**, Radiolysis of ammonia-containing ices by energetic, heavy, and highly charged ions inside dense astrophysical environments. **Astron. Astrophys. 509**, A87 (2010). doi: 10.1051/0004-6361/200912274
54. C. J. Hansen, D. A. Paige, L. A. Young, Pluto's climate modeled with new observational constraints. **Icarus 246**, 183–191 (2015). doi: 10.1016/j.icarus.2014.03.014
55. O. J. Tucker, R. E. Johnson, L. A. Young, Gas transfer in the Pluto-Charon system: A Charon atmosphere. **Icarus 246**, 291–297 (2015). doi: 10.1016/j.icarus.2014.05.002

ACKNOWLEDGMENTS

This work was supported by NASA's New Horizons Project. Additional support was provided by the Centre National d'Etudes Spatiales through its "Système Solaire" program (E.Q., S. Philippe, and B.S.). S.A.S. is also affiliated with Florida Space Institute, Uwingu LLC, Golden Spike Co., and World View Enterprises. As contractually agreed to with NASA, fully calibrated New Horizons Pluto system data will be released via the NASA Planetary Data System at https://pds.nasa.gov/ in a series of stages in 2016 and 2017 as the data set is fully downlinked and calibrated.

SUPPLEMENTARY MATERIALS

www.sciencemag.org/content/351/6279/aad9189/suppl/DC1
Supplementary Text
Figs. S1 to S6
Reference (**56**)

21 November 2015; accepted 12 February 2016
10.1126/science.aad9189

Surface compositions across Pluto and Charon

W. M. Grundy *et al.*

Science **351**, (2016);
DOI: 10.1126/science.aad9189